2024 IEEE International Conference on Robotics and Automation (ICRA 2024)
May 13-17, 2024. Yokohama, Japan

Acoustic Soft Tactile Skin (AST Skin)

Vishnu Rajendran S[1], Willow Mandil[1], Kiyanoush Nazari[1], Simon Parsons[1] and Amir Ghalamzan E.[2]

***Abstract*— This paper presents a novel acoustic soft tactile (AST) skin technology operating with sound waves. In this innovative approach, the sound waves generated by a speaker travel in channels embedded in a soft membrane and get modulated due to a deformation of the channel when pressed by an external force and received by a microphone at the end of the channel. The sensor leverages *regression* and *classification* methods for estimating the normal force and its contact location. Our sensor can be affixed to any robot part, e.g., end effectors or arm. We tested several regression and classifier methods to learn the relation between sound wave modulation, the applied force, and its location, respectively and picked the best-performing models for force and location predictions. The best skin configurations yield more than 93% of the force estimation within ±1.5 N tolerances for a range of 0-30^{+1} N and contact locations with over 96% accuracy. We also demonstrated the performance of AST Skin technology for a real-time gripping force control application.**

I. Introduction

Despite advancements in soft tactile sensing, persistent limitations are evident, as discussed in a recent review on tactile sensing technologies [1]. Many commercially available soft tactile sensors come with fixed shapes and sizes, posing challenges in integration with existing hardware, especially in space-constrained environments. For instance, incorporating camera-based tactile sensors is problematic due to their space requirements [2], [3]. Furthermore, developing sensors with intricate electrical components to fit tight spaces demands sophisticated manufacturing techniques and incurs high costs. There is a need for less complex tactile sensing technologies that can easily adapt to various shapes, limited space and form factors.

Accurate measurement of physical interactions plays a vital role in various physical robotic tasks, such as human-robot interaction [4], object grasping, and manipulation [5]. Tactile sensing can be used to observe the interaction state in physical robot interactions[6]. Tactile predictive models [7] can then make predictive controller possible, e.g. for slippage control [8] or cluster manipulation [9], leading to safer, more precise, and more efficient actions in a broader range of physical interaction tasks [7], [10], [11]. Soft tactile sensors are important for handling deformable objects and robust manipulation. These sensors feature a soft, flexible sensing surface whose deformation provides tactile information such as *normal/shear forces*, *contact location*, and contact surface texture, etc. Soft tactile sensors utilise both electronic (e.g., resistive [12], capacitive [13], piezoelectric [14], magnetic [15], [16], impedance [17]) and non-electronic transduction methods (e.g., camera-based [18], [19], [2], [20], [21], [22], [23], fluid-based [24], and acoustics [25], [26], [27], [28]) and their combinations [29] for converting the membrane deformation to tactile information.

Zoller et al. [31] proposed a simple concept for tactile sensing by using sound waves to a pneumatically actuated soft finger. They added a speaker and microphone within the finger's chamber. The microphone continuously monitors changes in sound modulation when the finger deforms due to an applied external force. They used the finger with added sensing capability to measure contact forces and contact location with precision [31], [32]. However, it is not a stand-alone sensor to be used on other robot counterparts.

Acoustic techniques have been explored earlier for deriving tactile features like contacts, deformations, forces, and shape recognition. For instance, Shinoda et al. [33] created a silicone hemispherical fingertip embedded with an ultrasound transmitter and receiver array, capable of detecting deformations up to 10 μm and inclination changes to 0.001 radians. They later added a hollow spherical cavity within the membrane to measure stress via acoustic resonance. Teramoto et al. [28] introduced a flexible membrane underlaid with acoustic transducers to measure object curvature upon contact. Tanaka et al. [27] devised an acoustic sensor for real-time lump detection in laparoscopic surgery, employing a silicone-based hollow tube and analysing the amplitude and phase difference of the sound waves when the tube encounters a lump.

Chuang et al. [25] designed an ultrasonic sensor capable of real-time static normal force measurements (1-6 N) and shape recognition, analyzing time-of-flight variations of ultrasonic pulses due to surface deformation. The sensor architecture includes a Thin Film Transistor layer sandwiched between piezoelectric PVDF layers and a soft polymer sensing surface. This design calls for sophisticated manufacturing. However, as outlined before, a revolution was brought by Zoller et al. [31], who simplified the use of acoustic methods to pinpoint the force, contact location and material characteristics using a soft pneumatic finger equipped with minimal acoustic hardware (a speaker and microphone). When featuring only a microphone, this sensing methodology can measure these tactile features [34]. These reports showcase the potential of using acoustic techniques to extract tactile information from soft material deformation. But for developing a low-cost tactile sensing skin, it is advisable (1) to avoid integrating complex electronic circuitry into the sensor membrane/skin and (2) relocating sensory hardware away from the sensing surface enables sensor compactness and avoids requiring sophisticated manufacturing techniques.

[1] University of Lincoln, Lincoln, UK [2] University of Surrey, Guildford, UK.

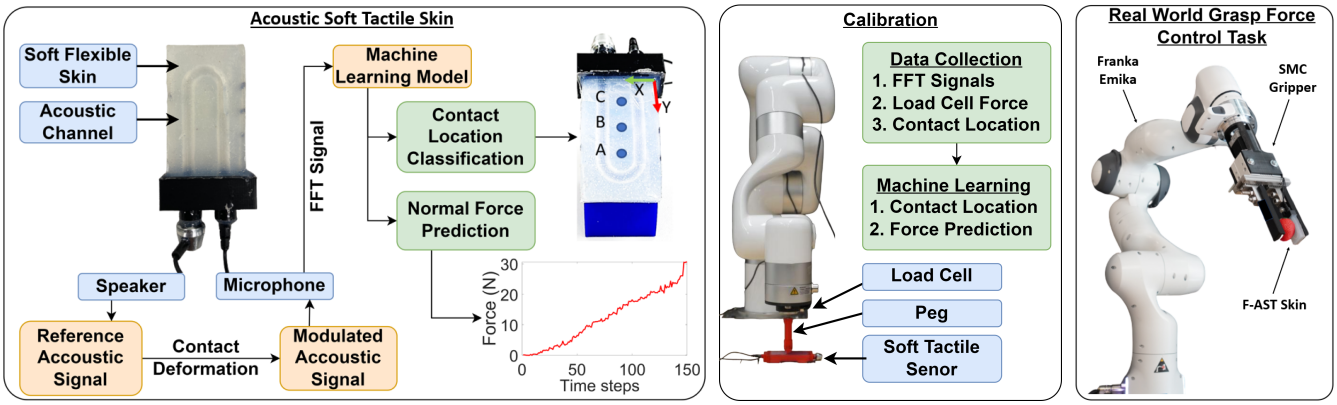

(a) (b) (c)

Fig. 1: AST Skin Overview (a): A force applied to the skin surface deforms the acoustic channels (ACs) beneath the sensing surface. These channels contain reference sound waves that travel from the speaker to the microphone. The sound wave amplitude is modulated in proportion to the deformation. We use FFT to transform the modulated waves to a frequency domain and machine learning methods to find the correlation between the modulations and (i) the contact normal force and (ii) the contact location resulting from the deformation. (b) Sensor calibration: the xARM robot is used to apply known forces to the AST skin at set locations through a load cell with a peg attached to the robot's wrist. The dataset contains the FFT signal, the load cell force values, and the contact location. ML models are trained with this dataset to predict the contact force and location. (c) We mounted this novel sensor on the SMC LEZH gripper to perform a grip force control pick-and-place task where it grips objects from the YCB object set [30] (a soft strawberry in this example), adapts grip force to reach a target force and then moves the object to a target location.

Further, this allows for a variety of skin form factors. With this ideology, we made AST skin [35], [36] a low-cost and easily manufacturable standalone soft tactile sensor.

This paper presents a stand-alone and low-cost tactile sensing technology suitable for being used in different shapes and sizes, called Acoustic Soft Tactile skin (**AST Skin**) (Fig. 1a). Our contribution includes (i) a novel open-source, low-cost tactile sensor that is easy to fabricate to fit different shapes. A flexible skin with embedded acoustic channels, a microphone, and speakers are the only key components of AST Skin, (ii) We also present a test design for a frameless AST (**f-AST**) for non-flat surfaces, (iii) We investigated different regression and classification methods for learning the relation between the applied force and its location and the microphone readings for our AST designs during its performance testing, (iv) We demonstrate the usability of AST Skin technology in robotic tasks by testing it on a non-flat surface and then on a gripper to perform force-controlled robotic pick-and-place tasks. These tests prove that AST technology can be used in realistic robotic applications.

II. Acoustic Soft Tactile Skin

a) Design: To prove the proposed AST Skin technology, we initially fabricated a flat, rectangular-shaped silicone skin measuring 35 mm x 60 mm. We mount the skin inside a 3D-printed casing to ensure portability and ease of testing and connecting the speaker-microphone unit. However, we have shown the skin design without a hard case in the later section of the paper. We investigated various skin configurations with single and dual acoustic channels (ACs) with simple geometrical shapes, such as cylindrical and conical, that run through the length of the skin. The diameter of the cylindrical AC is 5 mm, while the conical AC has diameters of 5 mm and 3 mm. The ACs connect the speaker-microphone arrangement of the skin. The prototyping procedure is detailed in the Appendix[1].

The speaker unit generates continuous sound waves that travel through the ACs, and the microphone receives the sound waves. As the channels deform due to external physical interactions, the amplitude of the sound waves changes (see Fig. 3), and we leverage ML models to capture the relationship between the amplitude changes and the tactile information. The details of the different skin configurations tested are presented in the following sections.

Acoustic Channel Design: The impact of contact deformation on sound waves varies with the shape of the ACs, which we exploit to estimate force and contact location. We investigated the effect of different channel configurations on feature extraction for force and contact location (see Fig 2 for AC designs).

We studied single-channel and dual-channel configurations to verify our hypothesis that ACs can be used to estimate tactile information. The study on single-channel skin configuration (AST 1) verifies the usability of this tactile skin, which calls for a narrow sensing region. For a broader sensing surface, the skin requires multiple channels, which we explore with studies on dual ACs (AST 2a-b, AST 3a-b, AST 4a-d) as an initial step. In future works, we will explore using multiple channels with different geometries spanning the entire skin area. For single-channel skin (AST 1), we considered a cylindrical-shaped channel. For dual channel skin configurations, we have used combinations of

[1]https://tinyurl.com/2mpy6vfr

(1) two cylindrical-shaped channels (AST 2a, AST 2b), (2) two conical-shaped channels (AST 3a, AST 3b), and (3) a conical-shaped channel with cylindrical-shaped one (AST 4a-4d).

By providing these channel configurations, we also tested two other design hypotheses: (1) Can AC with a non-varying cross-section (cylinder) distinguish forces acting on different points along their length? (2) for dual-channel skins, can ACs with different geometrical shapes (AST 4a-4d) best capture the tactile information compared to skins with similar AC geometries (AST 2a-2b, AST 3a-3b)?

Speaker Configurations: Speaker configurations are the second primary design feature we investigated in this work. We used a single speaker for AST 1, AST 2b, AST 3b, AST 4c, and AST 4d. We provided an individual speaker for each channel for AST 2a, AST 3a, and AST 4a-4b.
These speaker arrangements enable us to study the differences in skin performance (1) when all channels are provided with a single speaker versus each channel with an individual speaker and (2) when the speakers are arranged on the smaller and larger diameter ends of the conical channel (AST 4a and 4b, AST 4c and 4d). In this study, we used computer headphone speakers and a microphone, which will be replaced with a miniature type in further development studies.

A. Extracting Tactile Feature from Sound Signal

We aim to estimate two tactile features, i.e., the normal force (Newtons) and their contact location from the sound wave's amplitude modulation. We use the data-driven approach to capture the mapping between the sound's wave amplitude modulation and these features. First, we created a dataset using a robot arm and load cell by applying force to a series of locations on the soft skin. We then used different regression and classification methods to learn the mapping and outputting of the tactile features.

III. Experiments and Results

a) Sensor Calibration: We used a 6 DOF robot arm[2] with a calibrated load cell (Miniature In Line Load Cell, a high-precision axial load cell with 0-1 KN range and 10^{-5} N resolution) mounted on the robot wrist. It has an inbuilt driver board for USB communication with the PC and is mounted with a wedge-shaped 3D-printed peg as shown in Fig. 1b. We used the arm to apply known forces on AST Skin through the load cell and peg. We initially considered three calibration points on the skin surface for all configurations, namely $A = \{17, 50\}$, $B = \{17, 30\}$, and $C = \{17, 10\}$, as illustrated in Fig. 2j.

Each AST skin was positioned in a fixed location on the workbench for the calibration, as depicted in Fig. 1b, and a continuous reference sound signal was emitted through the speaker(s). The specific characteristics of this reference signal are outlined in the upcoming subsection. Subsequently, the robot arm approached each calibration point such that the peg exerted forces by an incremental push move of 0.2 mm. As the peg's central axis traversed vertically through the designated points, the AC(s) underwent compression. At every 0.2 mm increment, the corresponding load cell measurements were recorded, and simultaneously, the microphone captured 50 samples of the received sound signal. This procedure was repeated until the load cell reading reached 30^{+1} N (*, $*$ indicates the tolerance of the value) at each calibration points.

Reference Sound Signal: A test reference sound signal is generated using Audacity. It comprises four sine waves of frequencies of 300, 500, 700, and 900 Hz with an amplitude of 0.6 (on a 0 to 1 scale). During the sensor operation, this reference signal is played through the speaker(s).

Data Processing: The data processing pipeline for the calibration process is shown in Fig. 1b. After data processing, the resulting dataset contains the load cell readings with the corresponding contact location (A, B, or C) and the modulated sound waves' amplitudes and frequencies. We used Fast Fourier Transform (**FFT**) to compute the amplitudes of the sound signals received by the microphone (FFT data). For each skin model, 5100 data points are generated, with 1700 data points each for the three locations, A, B, and C.

A. Force and Contact Location Estimation:

We learned the amplitudes of individual frequency components in the reference signal (FFT data) vary with an increase in force from 0 to 30^{+1} N at each location A, B, and C on the AST Skin. Fig. 3 presents a sample of these variations for AST 1. This indicates the collected FFT data effectively could estimate unknown forces and their contact locations. Therefore, we express the unknown force and its location as:

$$(F_i, L_i) = f(A_{300,i}, A_{500,i}, A_{700,i}, A_{900,i}) \qquad (1)$$

where F_i is the unknown force at instance i, $A_{300,i}; A_{500,i}; A_{700,i}; A_{900,i}$ are the amplitudes of frequency components of the FFT at 300, 500, 700, and 900 Hz recorded at the same instance (FFT data), and L_i is the location of contact (A, B or C).

Performance Metrics: The following metrics present the outcomes of the tests conducted to present the findings. (i) We use validation error and accuracy for selecting regression and classifier models and each AST Skin configuration. (ii) The performance of force estimation is presented as the percentage of estimations that fall within $\pm$0.50 N, $\pm$1 N, and $\pm$1.50 N tolerance of the actual force values. (iii) The contact location estimation performance is presented as the total number of true estimations per test (170 trials are tested for each calibration points), and they are averaged to define the overall accuracy. We compared various regression and classifier models (see Appendix[1]) to estimate the force and its location from the FFT data. The models are trained using a dataset partition of 90:10 and 10-fold cross-validation. The *regression* model with the *minimum validation error* and the *classifier* with the *maximum accuracy* are selected for estimating force and location, respectively (refer to table I). The details of force and location estimations using these models are presented below.

[2]The UFactory xArm by ufactory.cc

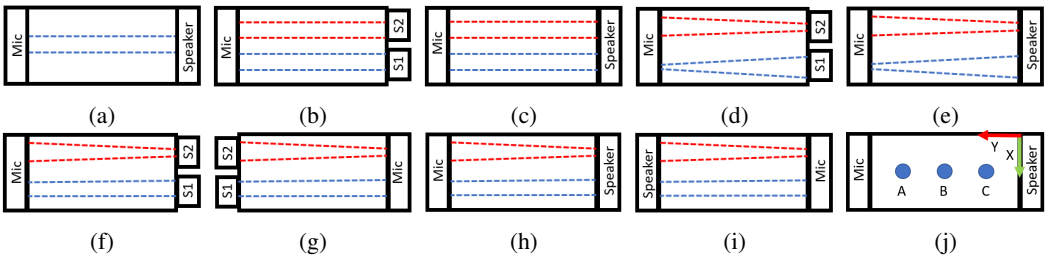

Fig. 2: AST Skin configurations tested: (a) AST 1 has a single channel; Double Channels: (b) AST 2a, (c) AST 2b, (d) AST 3a, (e) AST 3b, (f) AST 4a, (g) AST 4b, (h) AST 4c, (i) AST 4d; Calibration points selected for initial testing: $A = \{17, 50\}$, $B = \{17, 30\}$, and $C = \{17, 10\}$ (S1 and S2 refer to two speakers)

TABLE I: Regression and Classification models selected for various skin configurations (SVM: Support Vector Machines, GP: Gaussian Process, NN: Neural Network, KNN: K-Nearest Neighbors)

Skin Configuration	**Regression model**	**RMSE**	**Classifier model**	**Accuracy (%)**
AST 1	Exponential GP	0.72	Bagged Ensemble Trees	96.4
AST 2a	Rational Quadratic GP	2.21	Fine Guassian SVM	95.7
AST 2b	Matern 5/2 GP	3.24	Weighted KNN	98.2
AST 3a	Exponential GP	2.15	Bilayered NN	92.5
AST 3b	Exponential GP	1.06	Bagged Ensemble Trees	91.9
AST 4a	Exponential GP	3.25	Weighted KNN	92.8
AST 4b	Exponential GP	3.6	Fine Gaussian SVM	95.4
AST 4c	Exponential GP	2.53	Weighted KNN	97.2
AST 4d	Exponential GP	1.18	Weighted KNN	97.3

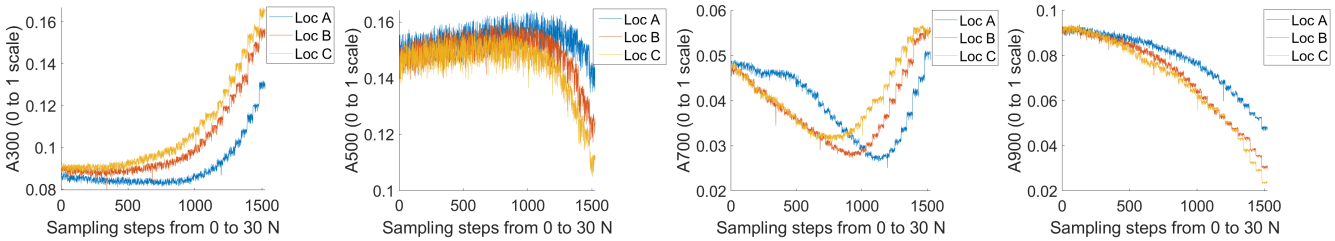

(a) 300 Hz component (b) 500 Hz component (c) 700 Hz component (d) 900 Hz component

Fig. 3: Variation of FFT data at locations A, B, and C on AST 1, when force varies from 0 to 30^{+1} N

Force estimation: The force estimation performance of the AST Skin configurations is presented in Fig. 4, showing the percentage of force estimations falling within ± 0.5 N, ± 1 N, and ± 1.5 N tolerances. The performance of each skin configuration is analysed based on the effect of AC geometries and speaker configuration.

1) Effect of Acoustic Channel Geometry: The single-channel AST 1 configuration demonstrated a force estimation accuracy of 82.74% within ± 0.5 N tolerance range and 93.5% within ± 1 N range, indicating that a single channel with a uniform geometrical shape can accurately infer contact forces acting on different points. Other skin configurations were also tested to investigate the feasibility of using an array of AC to serve a skin that may require a broader sensing surface area. The results in Fig. 4 show that considerably better performance can be achieved when the channel geometries are non-identical and a single speaker unit serves all channels. This is evident when comparing the performance of skin configuration AST 4d with other dual channel configurations.

2) Effect of Speaker Configuration: The results in Fig 4 indicate that the dual-channel skin configurations with a single speaker (AST 2b, AST 3b, AST 4c, AST 4d) mostly outperformed others or showed comparable performance to their dual speaker designs (AST 2a, AST 3a, AST 4a, AST 4b). This suggests that a single speaker can serve multiple channels without compromising performance. This finding can imply that the skin technology is potentially scalable, and a skin with multiple channels may not require an equal number of speakers (this is an open question for further validation in future). At the same time, positioning speakers on different ends of channels did not show any significant impact on the sensing performance.

Contact Location Estimation: Table II presents the accuracy of each AST configuration for estimating the contact locations (tested for 170 cases per location). All skin configurations achieved an accuracy greater than 89% for location estimation. The results in Table II also indicate that the performance of location estimation is better with a single speaker serving the AC(s).

TABLE II: Estimating the location of contact force for 170 test cases for points A, B, C

True predictions	**AST Skin configuration**								
	AST 1	AST 2a	AST 2b	AST 3a	AST 3b	AST 4a	AST 4b	AST 4c	AST 4d
A	169	169	168	165	163	168	168	168	168
B	160	168	169	150	142	151	156	165	167
C	164	153	168	161	150	155	162	166	162
Accuracy (%)	96.66	96.07	99.01	93.33	89.21	92.94	95.29	97.84	97.45

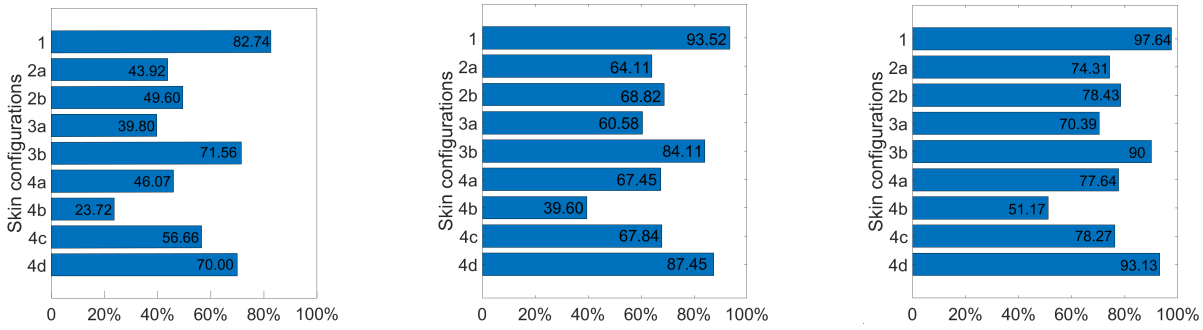

(a) ± 0.50 N tolerance (b) ± 1 N tolerance (c) ± 1.50 N tolerance

Fig. 4: Performance of different configurations of AST Skin: Percentage of force estimated with (a). ± 0.50 N, (b). ± 1 N, and (c). ± 1.50 N tolerance.

These results demonstrate (1) A smaller-width skin can utilise a single acoustic channel to accurately measure contact force and its location. The channel can have a simple geometry, such as a cylinder. Although the shape is fixed along its length, it can still distinguish forces and their locations applied at different points. (2) For skin with a broader sensing surface area, an array of non-identical ACs can be used, and individual speakers for each channel may not be necessary. (3) Further study will investigate AST with different AC shapes that may lead to improved AST performance and also use the cylindrical channel as loops to enhance the sensing area.

IV. Frame-less AST Skin

Frame-less AST (f-AST) Skin is the evolution of this AST concept, where it has a flexible sensing membrane capable of being fastened to any curved surface. This skin design can provide a broader range of robotic equipment with tactile sensation, such as enabling safer human-robot interactions in shared work environments. The test design of f-AST has a casing to house the speaker and microphone at the bottom and from which the sensing surface extends (refer Fig.5a). The acoustic channel design is cylindrical, connecting the speaker and microphone, inspired by AST 1 design which was the best-performing configuration. To test its capability of being used on curved surfaces for tactile sensing, the f-AST is attached to a 3D-printed curved surface, as shown in Fig.5b. The prototyping procedure is detailed in the Appendix[1].

To test the force and contact location capability, we employed a similar calibration process as used before. We chose three calibration points spaced 10 mm apart (while higher resolution calibration is feasible, it requires significantly more time) as illustrated in Fig.5a. A total of 6350 data points were collected, and we utilised a *90:10* data partitioning scheme for training and testing purposes. Here too, we evaluated various regression and classification methods, ultimately selecting the optimal model for estimating the force and its location. The Bagged Trees Ensemble exhibited the most promising cross-validation results, yielding a cross-validation error of 1.77 N for force estimation and a cross-validation accuracy of 99.2% for estimating force location. Fig.5c presents the percentage of accurately estimated forces with different tolerance values. Notably, 70.39% of force estimations fall within the ± 0.50 N tolerance range, while this percentage increases to 81.73%, 87.40%, and 89.60% within ± 1 N, ± 1.50 N and ± 2 N tolerances, respectively. AST demonstrates an impressive 99% accuracy for contact location estimation (Fig. 5d). These results show AST Skin technology can be used as a sensory cover for surfaces with different geometry needing tactile sensing.

TABLE III: Grip force control with f-AST Skin. The values in the table are the Mean Absolute Error (MAE) of the measured grip force by AST with respect to the desired grip force. The lower the MAE, the better the performance of the controller.

Target Grip Force	White Noise	Mean Absolute Error				
		Chess	Dice	Lemon	Marble	Strawberry
2 N	Off	0.03	0.04	0.04	**0.05**	0.02
	On	0.08	0.05	0.05	0.06	**0.09**
10 N	Off	0.26	0.14	0.38	0.40	**0.51**
	On	0.36	0.22	0.38	0.78	**0.91**
20 N	Off	0.40	**1.20**	0.40	0.73	0.19
	On	0.61	**1.10**	0.63	0.81	0.21

A. Noise Interference Test

We study the robustness of f-AST in the presence of white noise at 100 decibels for 0 N, 10 N, and 20 N constant

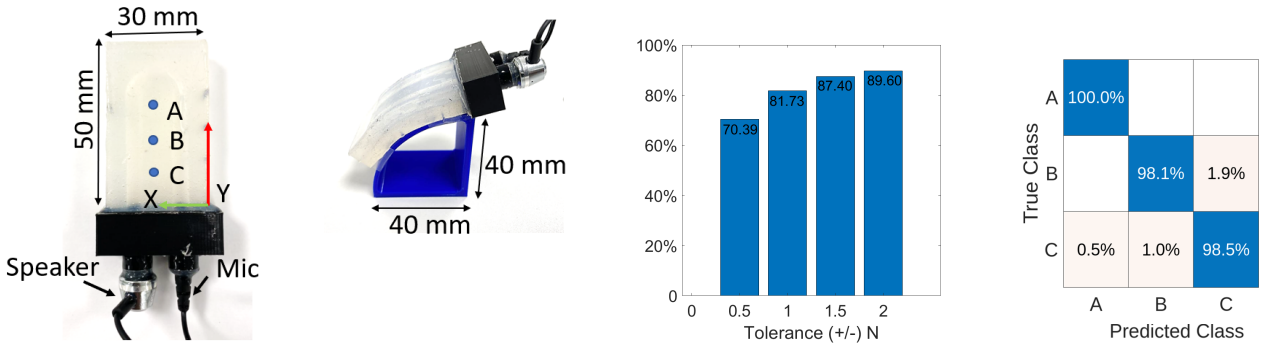

(a) (b) (c) (d)

Fig. 5: Frame-less AST Skin: (a) Frame-less AST (f-AST) Skin with calibration points: $A = \{15, 35\}$, $B = \{15, 25\}$, and $C = \{15, 15\}$ (b) skin mounted on the curved surface of a finger; (c); (d) Percentage of force estimations with $\pm$ 0.50 N, $\pm$ 1 N, and $\pm$ 1.50 N tolerance; (d) Contact location true predictions.

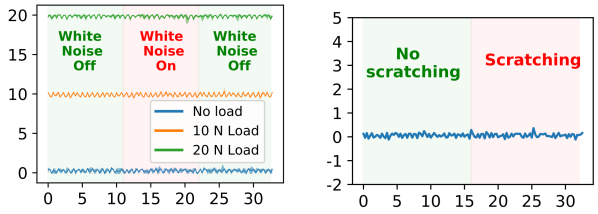

(a) (b)

Fig. 6: Noise interference tests (Force [N] vs time [s]). (a) f-AST Skin readings in the presence of white noise under no load and 10 N and 20 N loading conditions. (b) f-AST Skin readings when performing scratching on the sensor surface with a stiff paintbrush.

loading on point B. Fig 6a shows the sensor readings in the white noise tests. In test trials, we start with 11 seconds of normal conditions, then turn on the noise for the next 11 seconds, and finally return to normal conditions for the last 11 seconds. We repeated each loading test 5 times. Fig. 6a shows the mean and variance of the f-AST Skin reading, demonstrating it is robust to the white ambient noise. We also tested the effect of the contact noise on f-AST Skin readings by scratching the skin surface with no load condition with a stiff paintbrush for 11 seconds (Fig.6b). The figure shows that the sensor readings remain constant for smooth strokes compared to the normal no-load condition. Testing the contact noise effect under different loading conditions can be complex, as distinguishing the changes in f-AST Skin readings resulting from contact noise or from the actual contact forces may not be trivial.

B. Robotic Application

We tested the f-AST Skin in a pick-and-place task with real-time grip force control. We evaluated the performance of the controller by gripping five test objects from the YCB object set [30] with and without the presence of white noise (100 decibels). Fig. 1c shows an experimental setup consisting of (1) a seven dof Franka Emika arm, (2) an SMC LEZH gripper, and (3) an f-AST Skin. SMC gripper has a 30 mm stroke with a maximum of 210 N grip force. The control task includes (i) gripping an object from a top pose with a specified grip force, (ii) lifting the object upward 10 cm, (iii) moving it to a goal point, and (iv) dropping it there. The grip force controller aims to keep the grip force constant during stages using the f-AST Skin's tactile feedback. When the robot reaches the grip pose, the gripper starts decreasing its grip width with a 1 mm step size until the measured grip force by the f-AST Skin reaches a target desired value. Then, the lift, move, and drop stages are executed automatically. We tested the controller for three target grip forces, namely 2 N, 10 N, and 20 N.

Table III shows the Mean Absolute Error (MAE) of the target grip forces per object, and they are in the acceptable range for an early-stage prototype. The target force is based on the f-AST Skin readings and not a true contact force from a load cell. For 2 N and 10 N target grip forces, strawberry resulted in the highest MAE. For 20 N, the dice show the highest MAE. This is because these contact shapes are not in the calibration data set. However, this can be covered by an extensive calibration dataset. The table also shows that although the MAE in the reading during the white noise can be slightly higher than the normal test condition, they are very close to the desired force value.

V. Conclusion

We presented the concept of AST Skin based on sound wave amplitude modulation. AST Skin uses Acoustic Channels beneath the sensing surface to measure the contact normal force and its location. To validate the concept, we studied AST Skin designs with different configurations of acoustic channels, and acoustic hardware (speaker-mic) to validate the concept. The best AST Skin configurations made more than 93% of static normal force estimations with $\pm$1.5 N tolerance for a full-scale force range of 0-30^{+1} N and also made more than 96% accurate force contact location estimations. Moreover, we made a prototype of a frame-less AST (f-AST) Skin which demonstrated the potential for using it as a tactile sensory cover on curved surfaces and for real-time robotic applications. Overall, the AST Skin technology has the potential to become a valuable tool for tactile measurements for various robotic applications.

REFERENCES

[1] W. Mandil, V. Rajendran, K. Nazari, and A. Ghalamzan-Esfahani, "Tactile-sensing technologies: Trends, challenges and outlook in agri-food manipulation," *Sensors*, vol. 23, no. 17, p. 7362, 2023.

[2] W. Yuan, S. Dong, and E. H. Adelson, "Gelsight: High-resolution robot tactile sensors for estimating geometry and force," *Sensors*, vol. 17, no. 12, p. 2762, 2017.

[3] N. F. Lepora, "Soft biomimetic optical tactile sensing with the tactip: A review," *IEEE Sensors Journal*, vol. 21, no. 19, pp. 21 131–21 143, 2021.

[4] M. Fritzsche, N. Elkmann, and E. Schulenburg, "Tactile sensing: A key technology for safe physical human robot interaction," in *Proceedings of the 6th International Conference on Human-robot Interaction*, 2011, pp. 139–140.

[5] H. Yousef, M. Boukallel, and K. Althoefer, "Tactile sensing for dexterous in-hand manipulation in robotics—a review," *Sensors and Actuators A: physical*, vol. 167, no. 2, pp. 171–187, 2011.

[6] K. Nazari, W. Mandill, M. Hanheide, and A. G. Esfahani, "Tactile dynamic behaviour prediction based on robot action," in *Towards Autonomous Robotic Systems: 22nd Annual Conference, TAROS 2021, Lincoln, UK, September 8–10, 2021, Proceedings 22*. Springer, 2021, pp. 284–293.

[7] W. Mandil, K. Nazari, and A. Ghalamzan, "Action Conditioned Tactile Prediction: case study on slip prediction," in *Proceedings of Robotics: Science and Systems*, New York City, NY, USA, 6 2022.

[8] K. Nazari, W. Mandil, and A. M. G. Esfahani, "Proactive slip control by learned slip model and trajectory adaptation," in *Conference on Robot Learning*. PMLR, 2023, pp. 751–761.

[9] K. Nazari, G. Gandolfi, Z. Talebpour, V. Rajendran, P. Rocco *et al.*, "Deep functional predictive control for strawberry cluster manipulation using tactile prediction," *arXiv preprint arXiv:2303.05393*, 2023.

[10] R. S. Dahiya, G. Metta, M. Valle, and G. Sandini, "Tactile sensing—from humans to humanoids," *IEEE transactions on robotics*, vol. 26, no. 1, pp. 1–20, 2009.

[11] J. Dargahi and S. Najarian, "Advances in tactile sensors design/manufacturing and its impact on robotics applications–a review," *Industrial Robot: An International Journal*, 2005.

[12] J. Zimmer, T. Hellebrekers, T. Asfour, C. Majidi, and O. Kroemer, "Predicting grasp success with a soft sensing skin and shape-memory actuated gripper," in *2019 IEEE/RSJ International Conference on Intelligent Robots and Systems (IROS)*. IEEE, 2019, pp. 7120–7127.

[13] Q. Li, Z. Ullah, W. Li, Y. Guo, J. Xu, R. Wang, Q. Zeng, M. Chen, C. Liu, and L. Liu, "Wide-range strain sensors based on highly transparent and supremely stretchable graphene/ag-nanowires hybrid structures," *Small*, vol. 12, no. 36, pp. 5058–5065, 2016.

[14] K. Song, S. H. Kim, S. Jin, S. Kim, S. Lee, J.-S. Kim, J.-M. Park, and Y. Cha, "Pneumatic actuator and flexible piezoelectric sensor for soft virtual reality glove system," *Scientific reports*, vol. 9, no. 1, p. 8988, 2019.

[15] M. Rehan, M. M. Saleem, M. I. Tiwana, R. I. Shakoor, and R. Cheung, "A soft multi-axis high force range magnetic tactile sensor for force feedback in robotic surgical systems," *Sensors*, vol. 22, no. 9, p. 3500, 2022.

[16] G. Diguet, J. Froemel, M. Muroyama, and K. Ohtaka, "Tactile sensing using magnetic foam," *Polymers*, vol. 14, no. 4, p. 834, 2022.

[17] H. Wu, B. Zheng, H. Wang, and J. Ye, "New flexible tactile sensor based on electrical impedance tomography," *Micromachines*, vol. 13, no. 2, p. 185, 2022.

[18] B. Ward-Cherrier, N. Pestell, L. Cramphorn, B. Winstone, M. E. Giannaccini, J. Rossiter, and N. F. Lepora, "The tactip family: Soft optical tactile sensors with 3d-printed biomimetic morphologies," *Soft robotics*, vol. 5, no. 2, pp. 216–227, 2018.

[19] D. F. Gomes and S. Luo, "Geltip tactile sensor for dexterous manipulation in clutter," in *Tactile Sensing, Skill Learning, and Robotic Dexterous Manipulation*. Elsevier, 2022, pp. 3–21.

[20] E. Donlon, S. Dong, M. Liu, J. Li, E. Adelson, and A. Rodriguez, "Gelslim: A high-resolution, compact, robust, and calibrated tactile-sensing finger," in *2018 IEEE/RSJ International Conference on Intelligent Robots and Systems (IROS)*. IEEE, 2018, pp. 1927–1934.

[21] M. Lambeta, P.-W. Chou, S. Tian, B. Yang, B. Maloon, V. R. Most, D. Stroud, R. Santos, A. Byagowi, G. Kammerer *et al.*, "Digit: A novel design for a low-cost compact high-resolution tactile sensor with application to in-hand manipulation," *IEEE Robotics and Automation Letters*, vol. 5, no. 3, pp. 3838–3845, 2020.

[22] Z. Chen, S. Zhang, S. Luo, F. Sun, and B. Fang, "Tacchi: A pluggable and low computational cost elastomer deformation simulator for optical tactile sensors," *IEEE Robotics and Automation Letters*, vol. 8, no. 3, pp. 1239–1246, 2023.

[23] C. Sferrazza and R. D'Andrea, "Design, motivation and evaluation of a full-resolution optical tactile sensor," *Sensors*, vol. 19, no. 4, p. 928, 2019.

[24] D. Gong, R. He, J. Yu, and G. Zuo, "A pneumatic tactile sensor for co-operative robots," *Sensors*, vol. 17, no. 11, p. 2592, 2017.

[25] C.-H. Chuang, H.-K. Weng, J.-W. Chen, and M. O. Shaikh, "Ultrasonic tactile sensor integrated with tft array for force feedback and shape recognition," *Sensors and Actuators A: Physical*, vol. 271, pp. 348–355, 2018.

[26] H. Shinoda, K. Matsumoto, and S. Ando, "Acoustic resonant tensor cell for tactile sensing," in *Proceedings of International conference on Robotics and Automation*, vol. 4. IEEE, 1997, pp. 3087–3092.

[27] Y. Tanaka, T. Fukuda, M. Fujiwara, and A. Sano, "Tactile sensor using acoustic reflection for lump detection in laparoscopic surgery," *International journal of computer assisted radiology and surgery*, vol. 10, pp. 183–193, 2015.

[28] K. Teramoto and K. Watanabe, "Acoustical tactile sensor utilizing multiple reflections for principal curvature measurement," in *SICE 2001. Proceedings of the 40th SICE Annual Conference. International Session Papers (IEEE Cat. No. 01TH8603)*. IEEE, 2001, pp. 339–344.

[29] K. Park, H. Yuk, M. Yang, J. Cho, H. Lee, and J. Kim, "A biomimetic elastomeric robot skin using electrical impedance and acoustic tomography for tactile sensing," *Science Robotics*, vol. 7, no. 67, p. eabm7187, 2022.

[30] B. Calli, A. Walsman, A. Singh, S. Srinivasa, P. Abbeel, and A. M. Dollar, "Benchmarking in manipulation research: The ycb object and model set and benchmarking protocols," *arXiv preprint arXiv:1502.03143*, 2015.

[31] G. Zöller, V. Wall, and O. Brock, "Active acoustic contact sensing for soft pneumatic actuators," in *2020 IEEE International Conference on Robotics and Automation (ICRA)*. IEEE, 2020, pp. 7966–7972.

[32] V. Wall, G. Zöller, and O. Brock, "Passive and active acoustic sensing for soft pneumatic actuators," *arXiv preprint arXiv:2208.10299*, 2022.

[33] H. Shinoda and S. Ando, "A tactile sensor with 5-d deformation sensing element," in *Proceedings of IEEE International Conference on Robotics and Automation*, vol. 1. IEEE, 1996, pp. 7–12.

[34] G. Zöller, V. Wall, and O. Brock, "Acoustic sensing for soft pneumatic actuators," in *2018 IEEE/RSJ International Conference on Intelligent Robots and Systems (IROS)*. IEEE, 2018, pp. 6986–6991.

[35] V. R. S, S. Parsons, and A. G. E., "Acoustic soft tactile skin: Towards continuous tactile sensing," in *2023 21st International Conference on Advanced Robotics (ICAR)*, 2023, pp. 621–626.

[36] V. Rajendran, P. Simon, and A. G. E, "Single and bi-layered 2-d acoustic soft tactile skin," *International Conference on Soft Robotics (ROBOSOFT)*, 2024.